

High and Low Resolution Tradeoffs in Roadside Multimodal Sensing

Shaozu Ding^{1*}, Yihong Tang^{2*}, Marco De Vincenzi¹, and Dajiang Suo^{1†}

Abstract—Designing roadside sensing for intelligent transportation applications requires balancing cost and performance, especially when choosing between high and low-resolution sensors. The tradeoff is challenging due to sensor heterogeneity, where different sensors produce unique data modalities due to varying physical principles. High-resolution LiDAR offers detailed point cloud, while 4D millimeter-wave radar, despite providing sparser data, delivers velocity information useful for distinguishing objects based on movement patterns. To assess whether reductions in spatial resolution can be compensated by the informational richness of sensors, particularly in recognizing both vehicles and vulnerable road users (VRUs), we propose Residual Fusion Net (ResFusionNet) to fuse multimodal data for 3D object detection. This enables a quantifiable tradeoff between spatial resolution and information richness across different modalities.

Furthermore, we introduce a sensor placement algorithm utilizing probabilistic modeling to manage uncertainties in sensor visibility influenced by environmental or human-related factors. Through simulation-assisted ex-ante evaluation on a real-world testbed, our findings show marked marginal gains in detecting VRUs—an average of 16.7% for pedestrians and 11% for cyclists—when merging velocity-encoded radar with LiDAR, compared to LiDAR only configurations. Additionally, experimental results from 300 runs reveal a maximum loss of 11.5% and a average of 5.25% in sensor coverage due to uncertainty factors. These findings underscore the potential of using low spatial resolution but information-rich sensors to enhance detection capabilities for vulnerable road users while highlighting the necessity of thoroughly evaluating sensor modality heterogeneity, traffic participant diversity, and operational uncertainties when making sensor tradeoffs in practical applications. The code and data used in our experiments will be available at <https://github.com/ASU-Suo-Lab/Hi-Lo-Sensing>.

I. INTRODUCTION

Infrastructure-assisted sensing mechanisms have gained significant traction in recent years as promising solutions for improving transportation safety and efficiency. Data captured by roadside sensors can not only be used for traffic monitoring and control [1], [2], but can also be shared with connected vehicles to support vehicle-infrastructure cooperative perception and driving [3], [4]. Previous research has explored the deployment of single sensing modalities on the roadside to improve the perception of objects of interest, including LiDAR [5], [6], [7], cameras [8], and radar [9],

*Equal contribution

Technical support and review was provided by the Maricopa County Department of Transportation.

This work was partially supported by MIT Mobility Initiative.

¹The Polytechnic School, Arizona State University, Mesa, AZ 85212 USA sdling32@asu.edu, mdevinc2@asu.edu, dajiang.suo@asu.edu

²The University of Hong Kong, Hong Kong, China yihongt@connect.hku.hk

†Corresponding author: dajiang.suo@asu.edu

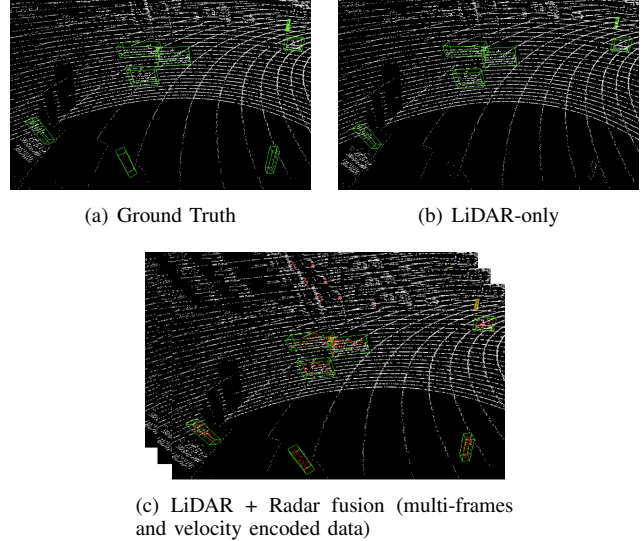


Fig. 1: Different detection performance on VRUs between high-resolution only and high-low combination sensing.

and roadside sensor in general [10]. However, achieving an optimal cost-performance tradeoff between high and low resolution remains challenging due to the physical heterogeneity among sensor types. For example, 4D millimeter-wave radar often generates a low-density point cloud to describe the 3D geometry of objects, compared to LiDAR, which produces a dense point cloud for each snapshot during the observation period (i.e., frame). However, radar can provide velocity-related information about objects, which, when aggregated over a longer temporal span, becomes useful in recognizing objects with varying movement patterns (e.g., fast-moving vehicles vs. slow-moving bicyclists and pedestrians). To leverage heterogeneous sensors to detect various traffic participants—each with unique shapes, sizes, and mobility levels—engineers must evaluate to what extent losses in spatial resolution in one sensor type can be compensated by the richness of information when choosing among different sensor configurations (e.g., LiDAR vs. 4D mmWave radar).

Additionally, LiDAR and radar signals attenuate differently depending on the propagation medium and surrounding environment. Deviations from intended installation positions due to human-related factors can also introduce uncertainties in the coverage areas of each sensor type, further complicating the tradeoff decision process. A pre-determined ‘optimal’ placement strategy does not always lead to precise installation as planned. To avoid the high costs associated with relocating or adjusting sensor placements, these uncertainties should be thoroughly evaluated prior to deployment.

This paper explores the tradeoff between high and low resolution in point cloud sensors for detecting heterogeneous traffic participants and determining their precise 3D locations, as shown in Fig. 1. Our key contributions are summarized as follows.

- **Multimodal sensor placement under uncertainty:** We propose a sensor deployment optimization algorithm that accounts for environmental and human-related uncertainties. The algorithm employs probabilistic modeling to characterize signal attenuation based on sensor-object distances, sensing modality, and surrounding environmental factors. By using a sampling-based approach to estimate sensor visibility regions with inherent randomness, the algorithm also considers potential deviations in planned installation positions and tilt angles, both of which can affect the coverage areas of roadside sensors.
- **Multimodal fusion neural networks cost-performance tradeoffs:** We design and implement a residual-based fusion deep neural network (DNN) to fuse LiDAR data, which provides a pure point cloud, with 4D mmWave radar data, which includes Doppler velocity of objects. The DNN-based fusion architecture enables a comprehensive evaluation of various roadside sensing solutions that combine different combinations of LiDAR and 4D mmWave radar data, each with varying levels of resolution, information richness (i.e., whether Doppler velocity is included), and temporal span (i.e., the number of frames used in fusion). The results quantify the tradeoff between spatial resolution and information richness across different sensing modalities.
- **Ex-ante evaluation of sensor deployment in a real-world intersection testbed:** We conduct an ex-ante evaluation of various sensor placement strategies, each involving different combinations of sensor types and resolutions, through a case study on a real-world intersection testbed developed by the authors. This evaluation leverages a realistic digital replica of the testbed, incorporating 3D road geometry, surrounding static objects that may occlude optical or millimeter-wave signals from roadside sensors, traffic and vulnerable road user flows from real-world scenarios, as well as potential locations and physical assets (e.g., traffic signal poles or masts) for sensor placement.

II. RELATED WORK

Previous studies have deployed roadside LiDARs and cameras to collect sensing information for autonomous driving perception. Chen et al. [11] proposed a non-model-based black-box optimization method to study radar networks deployment optimization in road environments. Based on light projection, Vijay et al. [12] used a regularized binary integer programming approach to optimize roadside sensors deployment in a simple 2D map. Daoudi et al. [13] described the sensor coverage optimization problem from the perspective of the mean and variance of unit visibility to maximize the area covered by a fixed number of sensors. However, most studies only optimize from the perspective of single-modal coverage and cost.

Advancements in sensor deployment and optimization improve 3D object detection, a key application in roadside sensing. Models like VoxelNet [14] and PointPillars [15] are widely used for efficient road user detection. To enhance accuracy, multimodal fusion strategies combine data from sensors like LiDAR, cameras, and radar. FusionRCNN integrates sparse LiDAR and dense camera data [16], M^2 -Fusion merges 4D radar and LiDAR for greater range and reliability [17], and EZFusion fuses radar, LiDAR, and camera for robust detection and tracking [18]. Incorporating temporal information from multiple frames of point cloud data also enhances detection. The MSF method [19] reduces computational redundancy by utilizing the motion of objects across frames. MVDNet improves bird’s-eye view vehicle detection in foggy conditions by fusing multi-frame LiDAR and radar signals [20]. Despite these advances, few studies have explored the trade-off between cost and performance when fusing high- and low-resolution sensors. This trade-off is critical for balancing accuracy and system cost in real-world applications.

III. SENSOR DEPLOYMENT OPTIMIZATION UNDER UNCERTAINTIES

Before evaluating different roadside sensing systems, each utilizing different combinations of sensing modalities and resolutions, we need to determine the coverage area of each sensor. We build on previous work [12], [21], [22] related to infrastructure LiDAR deployment by defining ‘sensor visibility,’ allowing us to quantify the coverage areas for each sensor. To put it formally, the road network is divided into a grid system to facilitate sensor deployment, where the region of interest (ROI) is represented as $R = \bigcup R_i$, with R_i being each road segment. To handle different sensor modalities, we define two sets of candidate points: one for LiDAR, $S^l = \{s_1^l, s_2^l, \dots, s_{N_l}^l\}$, and another for radar, $S^r = \{s_1^r, s_2^r, \dots, s_{N_r}^r\}$, where each s_i^l and s_i^r specifies a possible LiDAR and radar location, respectively. The target points, representing specific grid cells within the ROI that require monitoring, are denoted by $T = \{t_1, t_2, \dots, t_{N_T}\} \subset R$. Sensor visibility is captured using separate binary visibility matrices for each modality: $V^l \in \mathbb{R}^{N_l \times N_T}$ for LiDAR and $V^r \in \mathbb{R}^{N_r \times N_T}$ for radar. Here, $V_{i,j}^l = 1$ or $V_{i,j}^r = 1$ indicates that the respective LiDAR or radar sensor s_i can detect target point t_j , and $V_{i,j}^l = 0$ or $V_{i,j}^r = 0$ otherwise.

In previous work on simulation-based roadside deployment, the visibility condition checks whether a sensor’s beam reaches a point within a specified distance without being obstructed. If both conditions are met, the point is considered visible. Repeating this process for each sensor helps determine the overall coverage area for a given sensor setup. However, when merging multiple sensor types for real-world deployment, uncertainties arising from different signal attenuation and sensor degradation under various environmental conditions, or slight deviations in installation positions and orientations due to human-related constraints, may invalidate the previous assumptions about sensor visibility.

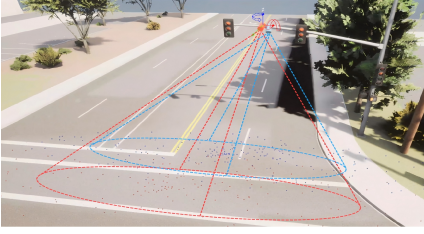


Fig. 2: The change in sensor visible region due to installation deviation. Red represents the expected visible area, while blue is the actual visible area caused by the deviation.

A. Multimodal Sensor Visibility under Uncertainties

To deal with these uncertainties that may influence sensor visibility, we enhance the previous sensor visibility conditions developed for LiDAR such that it can be adapted to multimodal settings, including 4D mmWave radar.

Environment uncertainties: Compared to the visibility condition developed for roadside LiDAR, which mainly determine whether a grid can be seen by a given sensor based on their distance, the visibility conditions for LiDAR and mmWave radar in real-world deployment varies and are subject to both the propagation medium and the surrounding environment. For example, with smaller wavelength, LiDAR’s signal degrades more rapidly than mmWave radar in the presence of airborne particles due to scattering. This can make a grid that is visible to a given LiDAR in clear air non-visible in heavy rain or fog. On the other hand, mmWave radar is prone to multi path effect that may incur either constructive or destructive interference with the latter reducing the strength of the received signal, increasing the chance of making certain grids non-visible. One way to tackle this is to build the sensing model for each sensor by considering its unique characteristics of signal propagation under various conditions [22]. As an alternative with lower cost, we present a generalized probabilistic model to characteristic the uncertainty nature of the sensor visibility condition under these effects, as shown in (1).

$$V_{i,j}^r = \begin{cases} \frac{1}{|S_j|} \sum_p e^{-\alpha \cdot d(s,p)}, & \{p \in S_j | d(p, t_j) \leq r\} \\ 0, & otherwise \end{cases} \quad (1)$$

In (1), $e^{-\alpha \cdot d(s,p)}$ represents the exponential decay of visibility based on the distance $d(s,p)$ between the sensor s and the target t_j and its neighbouring points p . The decay rate parameter α reflects the attenuation characteristics of each sensor. For LiDAR, α models the rapid signal degradation caused by scattering and absorption, particularly in adverse weather conditions where airborne particles disperse the light waves. In contrast, for mmWave radar, α encapsulates the impact of multipath effects, where reflected signals can interfere constructively or destructively, altering the overall signal strength.

The sum of all t_j neighbouring points in the numerator and the division by the size of the neighborhood $|S_i|$ is motivated by smoothing or averaging in probabilistic models. For LiDAR, if neighboring points suffer from heavy scattering, it’s

Algorithm 1 Sampling-based sensor visibility

Input: Number of sampling N , candidate points of LiDAR S_l and radar S_r , target grid set T .

Output: Visibility of LiDAR V^l and radar V^r .

```

1: Initialize Sensor visibility  $V^r, V^l \leftarrow \emptyset$ 
2: for  $i \leftarrow 1$  to  $N$  do
3:   Sample location deviation  $(x_i, y_i, z_i)$ , rotation deviation
    $(pitch_i, yaw_i, roll_i) \sim \mathcal{N}(\mu, \sigma^2)$ 
4:   for sensor  $x$  in {LiDAR, radar} do
5:     for  $s^x$  in  $S_x$  do
6:       Calculate sensor location  $L_x$ , rotation  $R_x \leftarrow$ 
        $s^x, (x_i, y_i, z_i), (pitch_i, yaw_i, roll_i)$ 
7:       Generate sensor point clouds  $\mathbb{P}_x \leftarrow L_x, R_x$ 
8:       Calculate overall sensor visibility  $V^x \leftarrow \mathbb{P}_x, T$ 
9:     end for
10:    end for
11: end for
12: return Average visibility  $V^r, V^l \leftarrow V^r/N, V^l/N$ 

```

more likely that the central target point will also experience reduced visibility, as the medium itself (like fog or dust) becomes increasingly opaque. For mmWave radar, due to the multipath effect, if neighboring points around the target are experiencing destructive interference (due to reflected signals arriving out-of-phase), it’s likely that the central target will also suffer reduced signal strength.

Human-related uncertainties: Even with a robust sensor placement strategy that accounts for the environmental uncertainties discussed above, the actual installation process by construction workers can lead to discrepancies in the expected visibility conditions of each roadside sensor, whether LiDAR or mmWave radar. Due to practical constraints, workers may not always able to install each sensor at the precise tilt angle or position as specified, resulting in deviations in the sensor’s visible region from the simulation results, as shown in Fig. 2.

Rather than simulating every possible deviation in installation position and orientation, motivated by previous work on determining roadside sensor performance under various uncertain factors arising from real-world operation [9], we propose a sampling-based algorithm (Algorithm 1) that employs Monte Carlo simulation to determine sensor visibility under installation deviation. By assuming that the deviations of sensor installation positions and orientation are small and can thus be approximated by a normal distribution $\mathcal{N}(\mu, \sigma^2)$, we can derive random samples to evaluate how well a sensor performs under the expected but minor deviations. The LiDAR and radar visibility obtained in each iteration are averaged separately and used as inputs to downstream tasks to optimize multi-modal sensor placement in Algorithm 2.

B. Multimodal Roadside Sensor Placement Optimization

With the goal of maximizing the visible region, we present an integer programming (IP) formulation to optimize multi-modal roadside sensor placement under budget constraints (Algorithm 2). The algorithm extends previous work on IP-based roadside LiDAR deployment [21] with key differences in the following aspects. First, Algorithm 2 takes into account the uncertainty factors that may influence sensor visibility.

Algorithm 2 Multi-modal Sensor Deployment

Input: Visibility of LiDAR V^l and radar V^r .

Output: Deployment points of LiDAR S_l and radar S_r .

$$\max \sum_j^{N_T} t_j \cdot \rho_j, \quad (2)$$

$$\text{s.t.} \sum_i^{N_l} x_i + \sum_i^{N_r} y_i \leq N \quad (3)$$

$$\sum_i^{N_l} -\ln(1 - V_{(i,j)}^l) \cdot x_i \geq t_j, \quad \forall j \in 1, \dots, N_T \quad (4)$$

$$\sum_i^{N_r} -\ln(1 - V_{(i,j)}^r) \cdot y_i \geq t_j, \quad \forall j \in 1, \dots, N_T \quad (5)$$

$$\rho_j = \left(\sum_i^{N_l} V_{(i,j)}^l x_i + \sum_i^{N_r} V_{(i,j)}^r y_i \right) \cdot w_j, \quad \forall j \in 1, \dots, N_T \quad (6)$$

$$x_i \in \{0, 1\}, \quad \forall i \in 1, \dots, N_l \quad (7)$$

$$y_i \in \{0, 1\}, \quad \forall i \in 1, \dots, N_r \quad (8)$$

$$t_j \in \{0, 1\}, \quad \forall j \in 1, \dots, N_T \quad (9)$$

The probabilistic sensor visibility grids derived from Algorithm 1 for both LiDAR V^l and mmWave radar V^r are used as inputs to Algorithm 2. Second, and more importantly, the sensor visibility conditions in Algorithm 2—denoted by (4) and (5)—imply that a given target grid (e.g., the j th grid) will not be considered visible unless it is “seen” by both LiDAR and radar. This redundancy constraint reduces the impact of the uncertainty factors on sensor visibility. The physical mechanisms behind signal attenuation differ between LiDAR and mmWave radar, making it less likely for a grid to be invisible to both sensors simultaneously compared to either sensor individually.

The objective of Algorithm 2 is to maximize the visible region in a probabilistic sense by accounting for uncertainty factors, as described in (2). The weight matrix ρ_j incorporates both the sensor visibility probability and the importance of each region or grid, as calculated by (6). For instance, if the goal of transportation monitoring is to detect potential conflicts between vehicles and vulnerable road users (VRUs) within the central region, a higher weight can be assigned to that area compared to the surrounding approaching lanes that connect to the intersection. The binary variables x_i and y_i represent candidate points for LiDAR and radar sensors, respectively. Equation (3) imposes a limit on the total number of sensors, representing a simplified form of the cost constraint.

IV. RESFUSIONNET FOR MULTIMODAL HIGH-LOW RESOLUTION FUSION

Algorithm 2 outlines sensor placement strategies for deploying multimodal sensors on roadside to capture data from road users. Using LiDAR and mmWave Radar, we explore whether reduced spatial resolution (e.g., lower point cloud density) can be compensated by information richness (e.g., velocity patterns). This is tested with ResFusionNet, a neural network extending PointPillars [15] to fuse multimodal sensing data across temporal spans, as shown in Fig. 3.

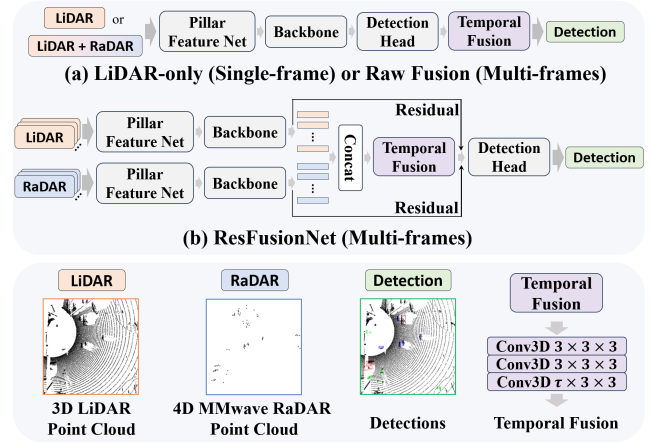


Fig. 3: The ResFusionNet architecture.

Fig. 3(a) illustrates the PointPillar network, and we refer to the method as LiDAR-only or Raw Fusion based on whether LiDAR point cloud is fused with radar point cloud at the input stage. Our ResFusionNet extends PointPillar to multimodal and multi-frame inputs. Specifically, we employ separate encoders (i.e., Pillar Feature Net and backbone) for each modality’s input. After encoding the data, we conduct feature fusion through concatenation before performing temporal fusion. To emphasize the importance of the most recently observed frame, we residually add the last frame’s feature to the output of the temporal fusion module. This design increases the network’s robustness and enables it to prioritize recent observations while still benefiting from the temporal context of earlier frames. ResFusionNet can be easily extended to handle more input modalities and frames, making it scalable for diverse sensor combinations and temporal spans. A detailed analysis of high and low-resolution tradeoffs using ResFusionNet’s detection results is provided in Sec. VI-C.

V. HIGH AND LOW-RESOLUTION TRADEOFF EXPLORATION THROUGH A REAL-WORLD CASE STUDY

The tradeoff between high and low-resolution sensing is investigated through a case study at an intersection testbed in Sun Lakes, Chandler, Arizona, USA. Due to the resort-like nature and numerous country clubs in Sun Lakes, this area experiences higher volumes of vulnerable road users (VRUs). The local Department of Transportation (DOT) seeks to improve its situational awareness to detect potential conflicts between vehicles and VRUs, to enhance safety. This motivates our exploration of cost-effective sensing solutions that can be scaled to other intersections with similar needs.

To minimize the costs of sensor relocation or reconfiguration, we utilize a simulation-assisted framework for ex-ante evaluation of sensor placement strategies with varying modalities and resolutions (Fig. 4). A realistic digital replica of the Sun Lakes testbed was built using publicly available data and input from stakeholders, including the local DOT.

- Digital maps of the intersection: We used GIS and aerial imagery to create an accurate map of the intersection, incorporating the road network and static objects (e.g.,

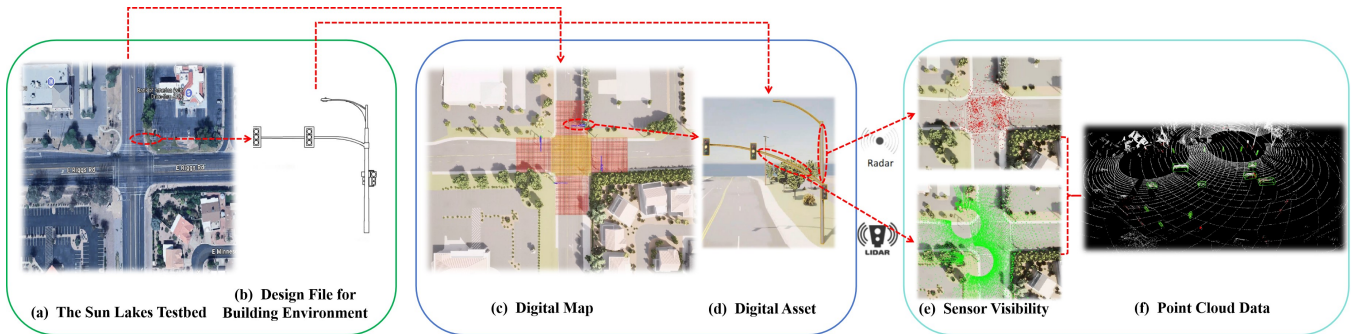


Fig. 4: Illustrating the ex-ante evaluation process through a case study on the Sun Lakes Test Bed in Sun Lakes, AZ, USA.

buildings, trees) using RoadRunner, a tool for 3D scene editing in autonomous vehicle applications.

- **Region of interest (ROI):** The central region (yellow in Fig. 4(c)) focuses on detecting vehicle and VRU conflicts. For different applications, such as adaptive traffic signal, the ROI may cover vehicle queues (red in Fig. 4(c)).
- **Potential sensor placement locations:** They were determined in consultation with the local DOT managing the intersection. While we are authorized to place sensors on traffic light poles at the intersection’s four corners, practitioners may select alternative locations to optimize visibility. In such cases, Algorithm 2’s sensor limit, based on procurement costs, can be adjusted to account for construction and maintenance costs (e.g., new poles, power, and communication lines). Discussions with domain experts revealed that pre-determined placement may not always be executed as planned due to positioning constraints, leading us to incorporate uncertainties into Algorithms 2.
- **Derivation of traffic and VRU flows for simulation:** Traffic engineers provided reasonable estimates of vehicle and VRU flows for the simulation. Alternative methods, such as using vehicle-generated movement data [23] or drone-captured aerial footage [24], can also be applied.

VI. EXPERIMENTAL RESULTS AND DISCUSSION

A. Experimental Settings.

In the experiment of sensor placement, we leverage CARLA [25] to explore feasible locations for placing sensors on traffic light poles in the four corners of the Sun Lakes testbed. The traffic light pole is divided into candidate points through linear interpolation with 330 candidate points for installing radars and 260 for LiDARs. Table I provides the sensor configurations with different modalities and resolutions used in our experiments. Algorithm 2 is executed by using Mixed Integer Programming Solver offered by the Gurobi, a mathematical programming toolbox. For each candidate point, we sample from a normal distribution $N(3, 1)$ to get the potential deviation from the planned installation locations and tilt angles. Drawing on the expertise of traffic engineers, the scene is configured to generate at least 44 cars, 40 bicycles, and 24 pedestrians per minute.

B. Sensor Placement under Uncertainties

Fig. 5 shows the coverage areas achieved by the proposed sensor placement algorithms (Algorithm 1 and Algorithm 2)

TABLE I: Sensor specifications and combinations.

Sensor Type	Resolution	Details	Cost
LiDAR	High	128 beams, 20Hz, 360° HFOV, 45° VFOV, $\leq 90m$	\$14k~15k
	Mid	64 beams, 20Hz, 360° HFOV, 45° VFOV, $\leq 90m$	\$6k~7k
	Low	16 beams, 20Hz, 360° HFOV, 30° VFOV, $\leq 100m$	\$4k~5k
Radar	High	20Hz, 120° HFOV, 28° VFOV, $\leq 90m$	\$7k~8k
	Low	20Hz, 130° HFOV, 15° VFOV, $\leq 95m$	\$1k~2k

Sensor Comb.	Type 1	Type 2	Type 3	Type 4	Type 5	Type 6
LiDAR radar	2×High 4×High	2×High 4×Low	2×Mid 4×High	2×Mid 4×Low	3×Low 3×High	3×Low 3×Low

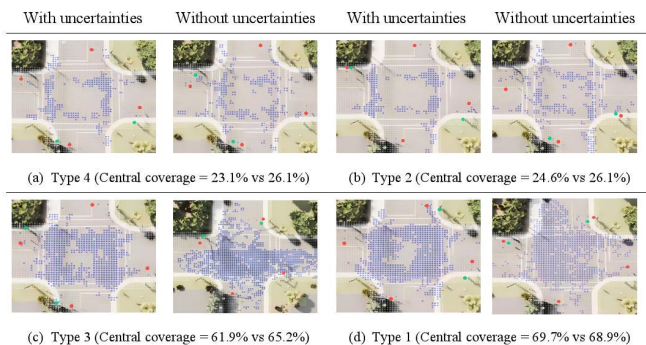


Fig. 5: Sensor visibility with and without uncertainties. Blue dots show visible target grids, red dots mark optimal radar locations, and green dots mark optimal LiDAR locations.

under different sensor configurations. The sensor placement algorithm that does not account for uncertainty factors is used as a benchmark. While in most cases (Fig. 5 a-c), the algorithm without considering uncertainty factors appears to achieve a higher coverage compared to the one incorporating uncertainty factors, it runs the risk of overestimating the sensor’s visible region. By accounting for signal attenuation for both LiDAR and mmWave radar under varying environmental conditions, as well as potential deviations in visible regions due to human-related installation constraints, the optimization that includes uncertainty imposes much stricter requirements to meet visibility conditions (4) and (5) in Algorithm 2.

In other words, the algorithm considering uncertainty factors addresses off-nominal cases where a grid may be

come invisible due to signal attenuation, whereas the algorithm without uncertainty assumes perfect signal propagation between sensors and the target object. Furthermore, the algorithm accounting for uncertainty is more robust; when one sensor’s coverage is compromised or offset due to environmental or human factors, its visibility can be compensated by other sensors. This is reflected in the results, where the coverage area achieved by considering uncertainty is more compact and concentrated in the central region, while the coverage without uncertainty is more dispersed and divergent.

C. 3D Object Detection for Traffic Participants

We assess the cost-performance tradeoffs by comparing the performance achieved by different sensor placements (Type 1-5 in Table I) on 3D object detection. The results from the proposed ResFusionNet and PointPillars (LiDAR-only) are given. Detection performance is measured using mean Average Precision (mAP) at two commonly used IoU thresholds, 0.25 and 0.7[26], as lower precision may suffice for tasks like traffic control [27], while tasks like motion prediction demand higher accuracy [28].

Fig. 6 shows the best detection results by ResFusionNet across different sensor combinations. Both ResFusionNet and LiDAR-only curves show that the most expensive sensor combination (Type 1) does not necessarily yield the highest accuracy, while Type 3 with lower cost often performs best. ResFusionNet consistently outperforms LiDAR-only, especially for VRUs. At an IoU threshold of 0.25, ResFusionNet (Type 6) exceeds the accuracy of any LiDAR-only setup for VRU detection, underscoring the importance of incorporating information-richness (velocity) from mmWave radar in recognizing smaller objects with irregular shapes and ResFusionNet’s effectiveness in extracting velocity-encoded features from raw data.

We further explore 3D detection results of ResFusionNet under three temporal span conditions ($\tau = 1, 3, \text{ and } 5$) in Fig. 7. Increasing the temporal span generally improves detection accuracies, although the optimal span can vary. We interpret that recognizing different objects becomes easier by

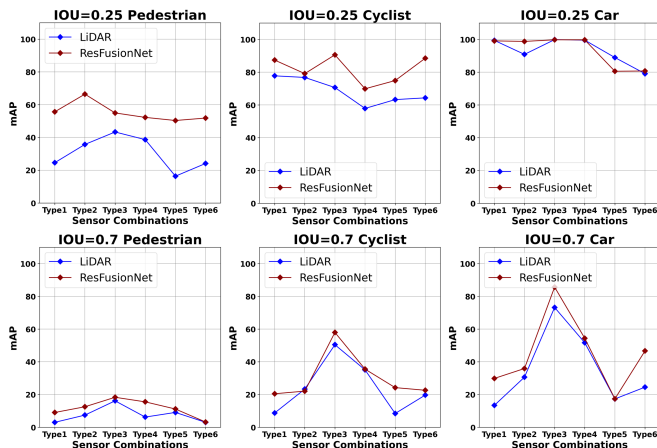


Fig. 6: 3D object detection results using different sensor combinations (costs gradually decrease from Type1 to Type6).

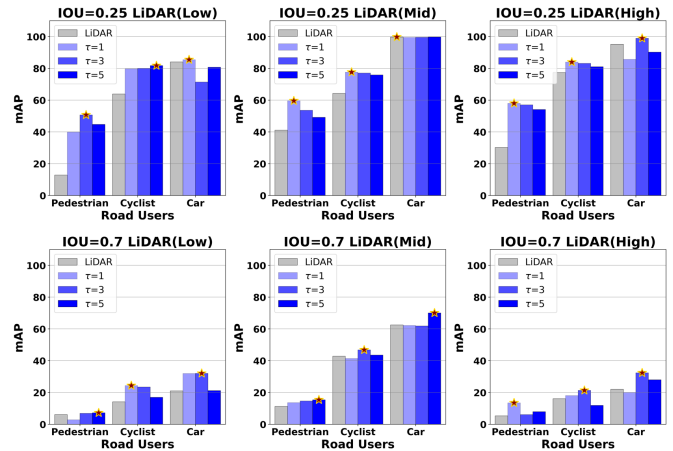


Fig. 7: Detection results of road users across different temporal spans under the feature fusion setting.

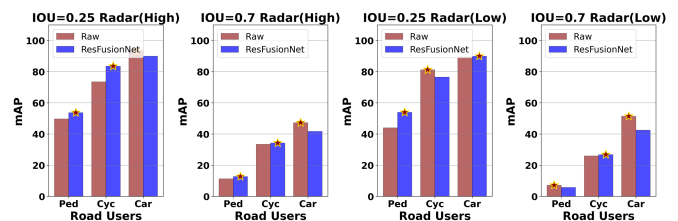


Fig. 8: Comparison between raw fusion (w/o velocity information) and feature fusion in ResFusionNet.

observing their movement patterns (e.g., changes in velocity) over a longer duration. An interesting observation is that for tasks not requiring high detection precision, $\tau = 1$ is often sufficient, while a longer temporal span benefit tasks demanding higher accuracy. This finding offers insights for balancing efficiency and accuracy in roadside sensing.

Fig. 8 compares Raw Fusion and ResFusionNet at a temporal span of $\tau = 3$. In general, ResFusionNet outperforms Raw Fusion in VRU detection, while no significant trend is observed for vehicles. This underscores the importance of feature-level fusion (performed by ResFusionNet) for heterogeneous sensing data. It is possible that merging LiDAR point cloud and radar velocity-encoded point cloud at the raw fusion level results in a loss of critical information, which is more essential for VRUs compared to vehicle detection.

VII. CONCLUSIONS

The experimental results underscore the potential of integrating low spatial-resolution, yet information-rich, sensors in roadside sensing systems to improve detection performance for vulnerable road users (VRUs) at a lower cost compared to relying exclusively on high-resolution solutions. However, for any real-world deployment, it is important to acknowledge that the extent of improvement in detecting VRUs by multimodal sensing solutions will also depend on factors such as the surrounding built environment and actual traffic flow. To manage expectations, we recommend that practitioners adopting our approach conduct a similar ex-ante evaluation process as outlined in Section V.

REFERENCES

- [1] Z. Bai, S. P. Nayak, X. Zhao, G. Wu, M. J. Barth, X. Qi, Y. Liu, E. A. Sisbot, and K. Oguchi, "Cyber mobility mirror: A deep learning-based real-world object perception platform using roadside lidar," *IEEE Transactions on Intelligent Transportation Systems*, vol. 24, no. 9, pp. 9476–9489, 2023.
- [2] J. Zhao, H. Xu, H. Liu, J. Wu, Y. Zheng, and D. Wu, "Detection and tracking of pedestrians and vehicles using roadside lidar sensors," *Transportation research part C: emerging technologies*, vol. 100, pp. 68–87, 2019.
- [3] R. Xu, J. Li, X. Dong, H. Yu, and J. Ma, "Bridging the domain gap for multi-agent perception," in *2023 IEEE International Conference on Robotics and Automation (ICRA)*. IEEE, 2023, pp. 6035–6042.
- [4] H. Xiang, Z. Zheng, X. Xia, R. Xu, L. Gao, Z. Zhou, X. Han, X. Ji, M. Li, Z. Meng *et al.*, "V2x-real: a large-scale dataset for vehicle-to-everything cooperative perception," *arXiv preprint arXiv:2403.16034*, 2024.
- [5] X. Cai, W. Jiang, R. Xu, W. Zhao, J. Ma, S. Liu, and Y. Li, "Analyzing infrastructure lidar placement with realistic lidar simulation library," in *2023 IEEE International Conference on Robotics and Automation (ICRA)*. IEEE, 2023, pp. 5581–5587.
- [6] A. Qu, X. Huang, and D. Suo, "Seip: Simulation-based design and evaluation of infrastructure-based collective perception," in *2023 IEEE 26th International Conference on Intelligent Transportation Systems (ITSC)*. IEEE, 2023, pp. 3871–3878.
- [7] W. Jiang, H. Xiang, X. Cai, R. Xu, J. Ma, Y. Li, G. H. Lee, and S. Liu, "Optimizing the placement of roadside lidars for autonomous driving," in *Proceedings of the IEEE/CVF International Conference on Computer Vision*, 2023, pp. 18 381–18 390.
- [8] Z. Zou, R. Zhang, S. Shen, G. Pandey, P. Chakravarty, A. Parchami, and H. X. Liu, "Real-time full-stack traffic scene perception for autonomous driving with roadside cameras," in *2022 International Conference on Robotics and Automation (ICRA)*. IEEE, 2022, pp. 890–896.
- [9] J.-K. Chen, M.-C. Lee, P.-C. Kang, and T.-S. Lee, "Roadside radar network deployment and parameter optimization in road environments," *IEEE Transactions on Vehicular Technology*, 2024.
- [10] Y. Ma, Y. Zheng, S. Wang, Y. D. Wong, and S. M. Easa, "Virtual-real-fusion simulation framework for evaluating and optimizing small-spatial-scale placement of cooperative roadside sensing units," *Computer-Aided Civil and Infrastructure Engineering*, vol. 39, no. 5, pp. 707–730, 2024.
- [11] J.-K. Chen, M.-C. Lee, P.-C. Kang, and T.-S. Lee, "Roadside radar network deployment and parameter optimization in road environments," *IEEE Transactions on Vehicular Technology*, vol. 73, no. 8, pp. 11 878–11 894, 2024.
- [12] R. Vijay, J. Cherian, R. Riah, N. De Boer, and A. Choudhury, "Optimal placement of roadside infrastructure sensors towards safer autonomous vehicle deployments," in *2021 IEEE International Intelligent Transportation Systems Conference (ITSC)*, 2021, pp. 2589–2595.
- [13] A. Daoudi, B. Detienne, R. E. Azouzi, I. Benelallam, and E. H. Bouyakhf, "Robust coverage optimization approach in wireless sensor networks," in *2017 International Conference on Wireless Networks and Mobile Communications (WINCOM)*, 2017, pp. 1–7.
- [14] Y. Zhou and O. Tuzel, "Voxelnet: End-to-end learning for point cloud based 3d object detection," in *Proceedings of the IEEE conference on computer vision and pattern recognition*, 2018, pp. 4490–4499.
- [15] A. H. Lang, S. Vora, H. Caesar, L. Zhou, J. Yang, and O. Beijbom, "Pointpillars: Fast encoders for object detection from point clouds," in *Proceedings of the IEEE/CVF conference on computer vision and pattern recognition*, 2019, pp. 12 697–12 705.
- [16] X. Xu, S. Dong, T. Xu, L. Ding, J. Wang, P. Jiang, L. Song, and J. Li, "Fusionrnn: Lidar-camera fusion for two-stage 3d object detection," *Remote Sensing*, vol. 15, no. 7, p. 1839, 2023.
- [17] L. Wang, X. Zhang, J. Li, B. Xu, R. Fu, H. Chen, L. Yang, D. Jin, and L. Zhao, "Multi-modal and multi-scale fusion 3d object detection of 4d radar and lidar for autonomous driving," *IEEE Transactions on Vehicular Technology*, vol. 72, no. 5, pp. 5628–5641, 2022.
- [18] Y. Li, J. Deng, Y. Zhang, J. Ji, H. Li, and Y. Zhang, "Ezfusion: A close look at the integration of lidar, millimeter-wave radar, and camera for accurate 3d object detection and tracking," *IEEE Robotics and Automation Letters*, vol. 7, no. 4, pp. 11 182–11 189, 2022.
- [19] C. He, R. Li, Y. Zhang, S. Li, and L. Zhang, "Msf: Motion-guided sequential fusion for efficient 3d object detection from point cloud sequences," in *Proceedings of the IEEE/CVF Conference on Computer Vision and Pattern Recognition*, 2023, pp. 5196–5205.
- [20] K. Qian, S. Zhu, X. Zhang, and L. E. Li, "Robust multimodal vehicle detection in foggy weather using complementary lidar and radar signals," in *Proceedings of the IEEE/CVF Conference on Computer Vision and Pattern Recognition*, 2021, pp. 444–453.
- [21] A. Qu, X. Huang, and D. Suo, "Seip: Simulation-based design and evaluation of infrastructure-based collective perception," in *2023 IEEE 26th International Conference on Intelligent Transportation Systems (ITSC)*, 2023, pp. 3871–3878.
- [22] X. Cai, W. Jiang, R. Xu, W. Zhao, J. Ma, S. Liu, and Y. Li, "Analyzing infrastructure lidar placement with realistic lidar simulation library," in *2023 IEEE International Conference on Robotics and Automation (ICRA)*. IEEE, May 2023. [Online]. Available: <http://dx.doi.org/10.1109/ICRA48891.2023.10161027>
- [23] W. Zhan, L. Sun, D. Wang, Y. Jin, and M. Tomizuka, "Constructing a highly interactive vehicle motion dataset," in *2019 IEEE/RSJ International Conference on Intelligent Robots and Systems (IROS)*, 2019, pp. 6415–6420.
- [24] O. Zheng, M. Abdel-Aty, L. Yue, A. Abdelraouf, Z. Wang, and N. Mahmoud, "Citysim: A drone-based vehicle trajectory dataset for safety-oriented research and digital twins," *Transportation Research Record: Journal of the Transportation Research Board*, vol. 2678, no. 4, p. 606–621, Jul. 2023. [Online]. Available: <http://dx.doi.org/10.1177/03611981231185768>
- [25] A. Dosovitskiy, G. Ros, F. Codevilla, A. Lopez, and V. Koltun, "Carla: An open urban driving simulator," in *Conference on robot learning*. PMLR, 2017, pp. 1–16.
- [26] X. Chen, H. Ma, J. Wan, B. Li, and T. Xia, "Multi-view 3d object detection network for autonomous driving," in *Proceedings of the IEEE conference on Computer Vision and Pattern Recognition*, 2017, pp. 1907–1915.
- [27] C. Chen, H. Wei, N. Xu, G. Zheng, M. Yang, Y. Xiong, K. Xu, and Z. Li, "Toward a thousand lights: Decentralized deep reinforcement learning for large-scale traffic signal control," in *Proceedings of the AAAI conference on artificial intelligence*, vol. 34, no. 04, 2020, pp. 3414–3421.
- [28] S. Ettinger, S. Cheng, B. Caine, C. Liu, H. Zhao, S. Pradhan, Y. Chai, B. Sapp, C. R. Qi, Y. Zhou *et al.*, "Large scale interactive motion forecasting for autonomous driving: The waymo open motion dataset," in *Proceedings of the IEEE/CVF International Conference on Computer Vision*, 2021, pp. 9710–9719.